RSC Advances

PAPER

View Article Online
View Journal | View Issue

Cite this: *RSC Adv.*, 2026, **16**, 19674

Functional integrated hydrogel with swelling–adhesion, antibacterial and conductive properties for acute wound hemostasis and diagnosis-treatment integration

Qin Wang,[ab] Linfeng Shi,[b] Yuqin Li,[bc] Xiuyu Liang,[d] Zhongnan Wang,[a] Gui Ma,[ab] Enke Feng,*[b] Zhiming Yang*[ab] and Lili Tian *[b]

Clinical wound management is severely hindered by delayed hemostasis, high infection risk, inefficient repair, and unregulated healing. Herein, a multifunctional KA-Ca^{2+}/Cu_2O@CuS composite hydrogel was fabricated using konjac glucomannan (KGM) and acrylamide (AM) cross-linked with Ca^{2+}, reinforced by Cu_2O@CuS nanoparticles. The most prominent superiority of this dynamic hydrogel over reported smart dressings lies in its rapid swelling-driven hemostatic performance, forming a synergistic system of "blood-triggered swelling occlusion-adhesive sealing-high-efficiency procoagulation" upon contact with wound exudate. *In vitro* assays demonstrated a 298% swelling ratio in tissue fluid, robust wet-tissue adhesion (26.3 kPa on porcine skin), rapid self-healing, and excellent biocompatibility (98% NIH3T3 cell survival). Cu_2O@CuS nanoparticles conferred broad-spectrum antibacterial activity (>91% inhibition against *Staphylococcus aureus* and *Escherichia coli*). *In vivo* rat tail amputation models verified rapid hemostasis (115 s) and accelerated wound healing (98.3% closure on day 12). Moreover, the hydrogel senses wound exudate and tearing, enabling "proof-of-concept exudate/strain monitoring". This multi-effect hydrogel holds great promise for clinical acute hemostasis, wound monitoring, and therapeutic intervention.

Received 23rd February 2026
Accepted 13th March 2026

DOI: 10.1039/d6ra01581f

rsc.li/rsc-advances

1 Introduction

Acute wounds resulting from trauma, surgical interventions, or accidental injuries are among the most common emergencies in clinical emergency care and surgical practice.[1,2] Efficient management of these wounds is directly pivotal to patients' life preservation, treatment duration, and post-healing outcomes.[3] Nevertheless, current acute wound management is still plagued by four interconnected and pressing core challenges, which have emerged as critical bottlenecks limiting clinical therapeutic efficacy: delayed hemostatic efficiency,[4] high wound infection susceptibility,[5–8] sluggish tissue repair progression,[9,10] and unregulated healing processes.[11,12] From a pathophysiological standpoint,[13] failure to achieve effective hemostasis promptly following acute wound occurrence can rapidly precipitate hemorrhagic shock. Subsequent to hemostasis, wounds are exposed to complex clinical settings and thus susceptible to invasion by pathogenic bacteria, such as *Staphylococcus aureus* and *Escherichia coli*. Bacterial colonization not only exacerbates local tissue necrosis but also may trigger systemic inflammatory response syndrome (SIRS) or sepsis *via* the systemic circulation, thereby further prolonging the treatment course.[14–16]

Although traditional wound care materials have been systematically applied in clinical practice, their monofunctional nature precludes simultaneous addressing of the aforementioned challenges, rendering them with notable performance limitations.[17,18] For instance, medical gauze, a staple in clinical settings, exhibits moderate blood-absorbing capacity and operational simplicity but suffers from poor conformability to irregular wound surfaces (*e.g.*, joint regions, deep lacerations).[19–21] Particularly in moist microenvironments with excessive wound exudate, it is prone to displacement or leakage, compromising hemostatic efficacy.[22] Studies have demonstrated that the hemostatic success rate of gauze on irregular wounds is approximately 60%; frequent replacement is therefore necessitated, which elevates the risks of secondary wound trauma and infection. While certain antibacterial materials can

[a]*Key Laboratory of Soil Ecological Health and Microbial Regulation, School of Resources, Environment and Life Sciences, Ningxia Normal University, Guyuan, 756009, China. E-mail: nxwangqin2018@163.com; 2025027@nxnu.edu.cn; nxsfxymg@163.com; yangzhiming1978@163.com*

[b]*Ningxia Key Laboratory of Green Catalytic Materials and Technology, College of Chemistry and Chemical Engineering, Ningxia Normal University, Guyuan, 756099, China. E-mail: tianlili@nxnu.edu.cn; 2428904251@qq.com; 1372036349@qq.com; NXSFEKF@163.com*

[c]*Lanzhou Bluestar Cleaning Co., Ltd, Lanzhou, 730060, China*

[d]*Department of Plastic Surgery, The First Affiliated Hospital of Xinjiang Medical University, Urumqi, 830054, China. E-mail: lxyskyer@163.com*

inhibit bacterial proliferation, they lack intrinsic procoagulant activity and thus fail to accelerate wound healing. More critically, these traditional materials are categorized as "passive care" modalities, incapable of real-time monitoring of physiological indicators during wound healing (wound exudate, temperature). Clinicians can only assess healing status through visual inspection or periodic sampling and testing, resulting in delays in treatment plan adjustments and impeding the achievement of individualized precision intervention.

To address the limitations of traditional materials, researchers have progressively shifted their focus to the development of multifunctional integrated[23,24–27] hydrogel dressings, aiming to concurrently achieve multiple functionalities[28–30]-including hemostasis,[31] antibacterial activity,[32] repair promotion, and monitoring–through the synergistic effects of constituent materials. However, a pervasive "performance trade-off" issue persists in the integration of multiple functionalities. For instance, high-concentration loading of antibiotics or nanoantibacterial particles to enhance antibacterial efficacy often compromises the cytocompatibility of hydrogels, resulting in reduced survival rates of fibroblasts and endothelial cells.[33,34] Similarly, the introduction of strong cross-linking sites to reinforce hydrogel adhesion to wound tissues tends to sacrifice material flexibility, rendering it difficult to accommodate dynamic movements at wound sites and even inducing secondary wound tearing during bodily activities. Furthermore, most current multifunctional hydrogels[35] are confined to the "therapeutic" realm, and the development of multifunctional composite hydrogels that integrate therapeutic functionalities with diagnostic capabilities (*e.g.*, real-time monitoring of wound status[36–39]) is still in its nascent stage. Such hydrogels fail to meet the clinical requirement for full-process management of acute wounds—namely, "rapid hemostasis, infection control, dynamic monitoring, and precise repair"—thereby significantly hindering their clinical translation and application.

Building on the aforementioned clinical challenges and current research landscape, this study precisely tailors material properties to meet wound repair requirements by selecting konjac glucomannan (KGM)[40] and acrylamide (AM) as components for constructing a composite matrix—KGM, a natural polysaccharide, boasts excellent biocompatibility, hydrophilicity, and inherent procoagulant potential to adapt well to the physiological wound healing microenvironment, while AM contributes favorable mechanical toughness and structural tunability, achieving synergistic optimization of natural materials' inherent biocompatibility and synthetic materials' structural stability; $CaCl_2$ is employed as the cross-linking agent to supply Ca^{2+}, which forms stable coordination bonds with oxygen-containing groups on KGM and AM molecular chains, and as an endogenous ion, it circumvents biosafety risks of exogenous cross-linking agents while enhancing the hydrogel's swelling capacity and adhesion stability; additionally, Cu_2O@CuS nanoparticles are loaded to establish a synergistic antibacterial system (reducing individual nanoparticle dosage to minimize cytotoxicity to normal cells) and endow conductive properties for wound monitoring, successfully fabricating a multifunctional composite hydrogel integrating swelling-adhesion and high-efficiency procoagulant activity that rapidly initiates a "blood-triggered swelling occlusion-adhesive sealing-high-efficiency procoagulation" mechanism upon contact with wound exudate, exhibits a 298% swelling ratio in tissue fluid, 26.3 kPa wet-tissue adhesion strength on porcine skin, rapid self-healing, 98% maximum NIH3T3 cell survival rate, over 91% inhibition rate against *Staphylococcus aureus* and *Escherichia coli*, and *in vivo* rat tail amputation assays confirm its superior hemostatic performance (115 s hemostatic time), accelerated wound healing (98.3% closure rate on day 12 post-treatment), and capability to sense wound exudate concentration and tearing to support integrated diagnosis and treatment, holding substantial application prospects in clinical hemostasis, healing monitoring, and acute wound therapeutic intervention as a multi-effect integrated wound repair material.

2 Results and discussion

2.1. Design and synthesis of the composite hydrogel KA-Ca^{2+}/Cu_2O@CuS

Fig. 1A illustrates the synthesis process of the composite hydrogel KA/Ca^{2+}/Cu_2O@CuS. Firstly, Cu_2O was sulfited to obtain Cu_2O@CuS, and Cu_2O@CuS nanocubes were successfully prepared by etching. The corresponding monomers acrylamide, glucomannan, and $CaCl_2$ were added to distilled water and dissolved to form a mixed solution. After Cu_2O@CuS was ultrasonically dispersed into the above mixed solution, ammonium persulfate (APS) was added. The mixture was poured into a mold and placed in an oven at 60 °C for gelation, resulting in the KA-Ca^{2+}/Cu_2O@CuS composite hydrogel (Fig. 1B).

In the synthesis process of the hydrogel, glucomannan serves as the main body of the gel. APS as an initiator to trigger the polymerization of acrylamide, and the cross-linking network is formed through the entanglement and interaction between polyacrylamide chains and glucomannan molecules. Hydrogen bonding interactions between the hydroxyl groups of glucomannan and the amino groups of polyacrylamide, thereby forming the KA-Ca^{2+}/Cu_2O@CuS composite hydrogel with high adhesiveness. The presence of $CaCl_2$ not only promotes gel formation but also exhibits excellent coagulation function, laying a solid foundation for wound hemostasis and healing. The multifunctional properties of the composite hydrogel are illustrated in Fig. 1C.

2.2. Structure and morphology analysis

The chemical composition of the KA-Ca^{2+}/Cu_2O@CuS composite hydrogel was characterized using Fourier transform infrared (FTIR). As shown in Fig. 2A, I, II, and III correspond to the infrared spectra of KGM powder, KA-Ca^{2+} hydrogel, and KA-Ca^{2+}/Cu_2O@CuS hydrogel, respectively. In I, the peak around 3415 cm^{-1} is attributed to the stretching vibration of –OH, the peak at 3142 cm^{-1} corresponds to the absorption of free $–NH_3$, and the peak at 1614 cm^{-1} may be the absorption of –C=O. The peak at 1406 cm^{-1} is assigned to $–CH_2$ absorption, while the peak at 1012 cm^{-1} arises from the bending vibration of alcoholic hydroxyl groups and the absorption of –C–O–.

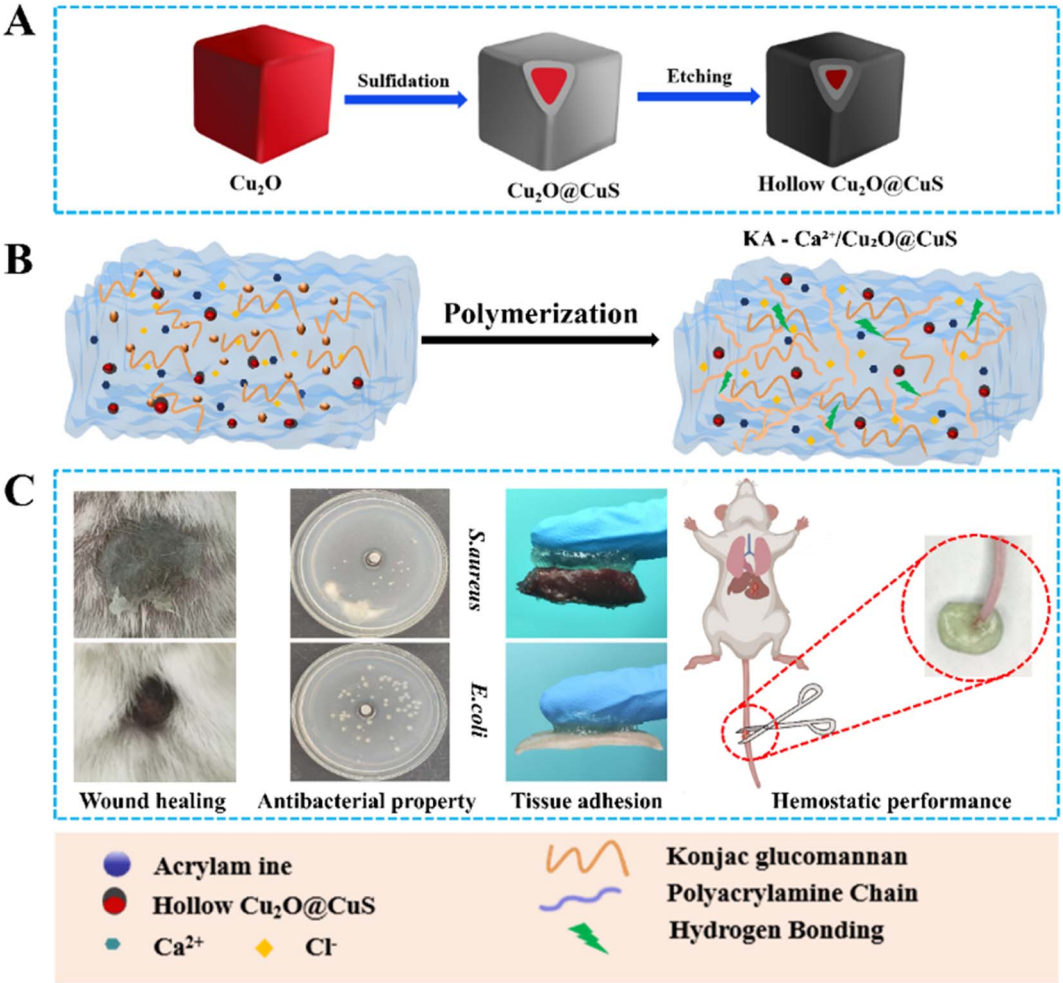

Fig. 1 Schematic of the fabrication process of KA-Ca^{2+}/Cu_2O@CuS composite hydrogel. (A) Preparation of/Cu_2O@CuS Nanocubes. (B) Preparation of composite hydrogels. (C) Multifunctional properties of KA-Ca^{2+}/Cu_2O@CuS composite hydrogels.

As presented in the FTIR spectrum, the absorption peak at 1012 cm^{-1} in region II was significantly enhanced, which is attributed to the increased number of –C–O– bonds formed during the coordination reaction between KA and Ca^{2+}. This result confirms the successful cross-linking of the hydrogel matrix, indicating that the coordination reaction between KA and Ca^{2+} proceeded smoothly. In region III, the absorption peak at 3415 cm^{-1}, which corresponds to the stretching vibration of –OH and –NH groups, exhibited an increasing trend. This phenomenon is mainly associated with the introduction of Cu_2O@CuS nanoparticles, as the interaction between Cu_2O@CuS and the hydrogel matrix can promote the exposure of free $–NH_2$ groups from polyacrylamide, thereby leading to the enhancement of peak intensity. Additionally, the relative intensity of the peak at 1406 cm^{-1}, assigned to the bending vibration of $–CH_2$ groups, was observed to increase. This change is reasonably ascribed to the structural rearrangement of the hydrogel matrix during the reaction process. Collectively, the FTIR characterization results provide strong evidence for the successful preparation of the Cu_2O@CuS nanocube-loaded composite hydrogel, and also verify the effective interaction between the components of the hydrogel system.

As displayed in Fig. 2B, the scanning electron microscopy (SEM) image of the KA-Ca^{2+}/Cu_2O@CuS composite hydrogel exhibits a distinct irregular grooved structure, which was attributed to the certain degree of shrinkage of the composite hydrogel during the freeze-drying process. Fig. 2C presents the X-ray photoelectron spectroscopy (XPS) spectra of the composite hydrogel, which was mainly composed of elements including C, O, Cu, N, and Ca. Fig. 2D reveals that element C exists predominantly in three chemical states: –C–O–, –C–C–, and O–C=O. In Fig. 2E, oxygen is mainly present in the forms of –C–O– and –C=O. Fig. 2F indicates that N primarily exists as $–C–NH_3$. As depicted in Fig. 2G, the Cu element is mainly present as cuprous oxide (Cu_2O). Fig. 2H shows that Ca is mainly in the forms of calcium ions (Ca^{2+}) and calcium oxide (CaO). In addition, energy-dispersive spectroscopy (EDS) mapping was performed to analyze the element distribution of the composite hydrogel, and the results are shown in Fig. 2I. The EDS mapping images clearly demonstrate the uniform distribution of the aforementioned elements in the hydrogel matrix, which further confirms the successful preparation of the KA-Ca^{2+}/Cu_2O@CuS composite hydrogel. It is worth noting that the Cl element exhibits a relatively non-uniform distribution, which is mainly

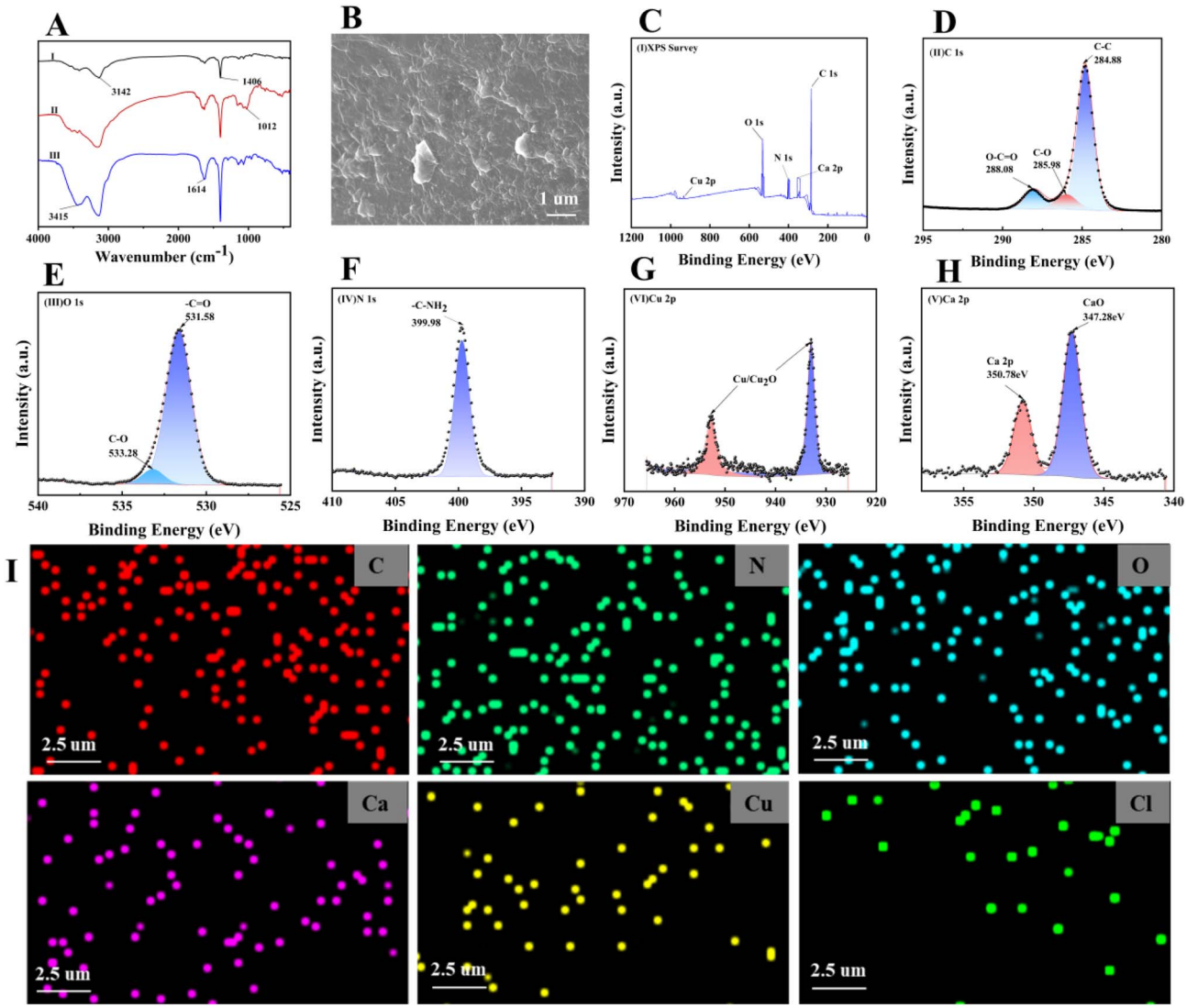

Fig. 2 (A) FTIR of KGM powder, KA-Ca^{2+}, KA-Ca^{2+}/Cu_2O@CuS composite hydrogels. (B) SEM of KA-Ca^{2+}/Cu_2O@CuS composite hydrogels. (C) XPS spectra of KA-Ca^{2+}/Cu_2O@CuS composite hydrogels. XPS of element in the composite hydrogel. (D) C. (E) O. (F) N. (G) Cu and (H) Ca. (I) EDS of the composite hydrogel.

attributed to the swelling–drying process of the hydrogel and the local aggregation of functional components during the formation of the three-dimensional network structure.

2.3. Self-healing properties of KA-Ca^{2+}/Cu_2O@CuS composite hydrogel

The frequency sweep curves of the hydrogel measured at 1% strain and 25 °C are displayed in Fig. 3A. Within the linear response range of 1–10 Hz, the KA-Ca^{2+}/Cu_2O@CuS composite hydrogel demonstrates stable elastic behavior. Notably, throughout the entire frequency sweep, the storage modulus (G') remains consistently higher than the loss modulus (G''), which confirms that the hydrogel behaves as an elastic solid with reliable stability.

The self-healing potential of hydrogels remarkably enhances the durability of wound dressings.[41,42] To assess the self-healing capability of the KA-Ca^{2+}/Cu_2O@CuS composite hydrogel, strain amplitude sweep measurements were conducted at 25 °C to explore its rheological response to external strain. As depicted in Fig. 3B, the KA-Ca^{2+}/Cu_2O@CuS composite hydrogel maintains network integrity until the strain reaches approximately 161%. This phenomenon is ascribed to the incorporation of AM, which constructs a dense hydrogen bond network within the hydrogel framework, thereby substantially augmenting the hydrogel's mechanical properties. Beyond this threshold, both the storage modulus (G') and loss modulus (G'') undergo a sharp decline and attain equilibrium–an observation that explicitly signifies hydrogel network disruption, with the material transitioning from a gel state to a sol–gel state upon exceeding the critical strain. Subsequently, the self-healing performance of the KA-Ca^{2+}/Cu_2O@CuS composite hydrogel was evaluated *via* consecutive cyclic strain tests (1% strain → 200% strain → 1% strain) at a fixed angular frequency of 10 rad s^{-1}. As shown in Fig. 3C, the hydrogel transitions to a sol–gel state ($G' < G''$) when

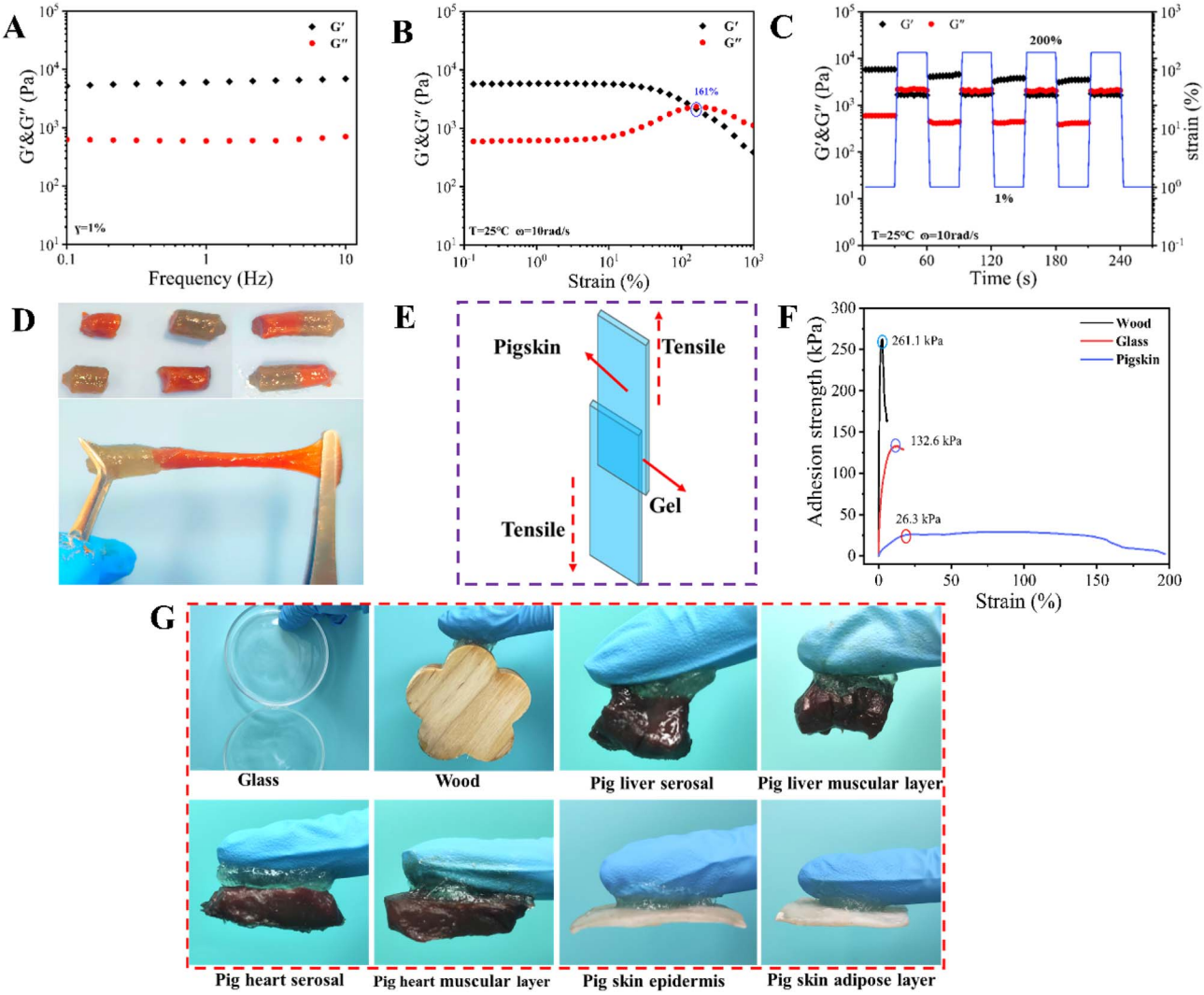

Fig. 3 Self-healing and adhesion performance of the KA-Ca^{2+}/Cu_2O@CuS composite hydrogel. (A) Frequency sweep. (B) Strain amplitude sweep. (C) Behavior of G' and G'' of the KA-Ca^{2+}/Cu_2O@CuS composite hydrogel as the shear strain shifts between 1 and 200% in steps. (D) Optical images of the self-healing process. (E) Schematic diagram of the lap shear test. (F) Adhesion strength on different substrates. (G) Adhesion performance of the composite hydrogel with different substrates.

the strain exceeds 200%. Upon strain restoration to 1%, the G' and G'' values immediately recover to their initial states, followed by seamless network reorganization. The rapid, reversible sol–gel transition behavior exhibited in the cyclic tests highlights the inherent, excellent self-healing characteristics of the hydrogel network.

Materials based on hydrogen bonding interactions can achieve structural reconstruction and performance recovery after damage through intermolecular or intramolecular interactions, with the core lying in the dynamic reversibility and responsiveness of hydrogen bonding interactions. In this system, a double network is formed by introducing polyacrylamide and $CaCl_2$ ionic liquid into the glucomannan network, and the hydrogen bonding interactions formed between them possess both stability and dynamic adjustability. These interactions are not permanent combinations but are in a dynamic equilibrium of "breakage-reconstruction", providing a solid structural foundation for the self-healing of the material.

Endowed by hydrogen bonding interactions, the composite hydrogel achieves remarkable self-healing capability at room temperature without the need for external stimuli. As depicted in Fig. 3D, a cylindrical composite hydrogel sample was cut into two halves, with one half stained. The cut surfaces were merely brought into simple contact without applying any pressure. After standing for 5 minutes, the sample formed an intact gel that could withstand stretching. This phenomenon is attributed to the rearrangement of reversible multiple hydrogen bonds, which facilitates the healing of the hydrogel.

2.4. Adhesion performance of KA-Ca^{2+}/Cu_2O@CuS composite hydrogel

Adhesion performance serves as a core indicator governing the fixation stability of wound dressings and the continuity of wound monitoring, which directly impacts therapeutic efficacy and patient safety during application.[43,44] In the present study,

the superior adhesiveness of the KA-Ca^{2+}/Cu_2O@CuS composite hydrogel to diverse substrates (Fig. 3G)stems from the dynamic cross-linked network fabricated among acrylamide (AM), konjac glucomannan (KGM), and calcium ions (Ca^{2+}). Leveraging the synergistic effects of hydrogen bonds and ionic bonds, this network not only reinforces the internal structural stability of the gel molecules but also confers the hydrogel with robust binding capacity to various wet substrates, particularly biological tissues.

To quantitatively characterize the adhesion strength of the composite hydrogel, lap shear tests were conducted (Fig. 3E).[45] As illustrated in Fig. 3F, under the dual effects of strong hydrogen bonds and ionic bonds, the KA-Ca^{2+}/Cu_2O@CuS composite hydrogel demonstrates stable adhesive performance on three typical substrates (porcine skin, glass, and wood), with measured adhesion strengths of 26.3 kPa, 132.6 kPa, and 261.1 kPa, respectively. Among these substrates, porcine skin-employed as a standard substrate for simulating human skin tissue-exhibits an adhesion strength that is directly correlated with the hydrogel application potential as a wound dressing.

As documented in relevant literature,[46] the adhesion strength between wound dressings and porcine skin must reside within a specific range to balance fixation efficacy and application safety: adhesion strength below 8 kPa renders the dressing susceptible to displacement or detachment during patients' daily activities, compromising continuous wound coverage and the exertion of hemostatic, antibacterial, and other essential functions; conversely, adhesion strength exceeding 32 kPa may lead to epidermal tearing of the wound during dressing replacement, thereby inducing secondary injury. In the present study, the adhesion strength of the KA-Ca^{2+}/Cu_2O@CuS composite hydrogel to porcine skin (26.3 kPa) falls precisely within the optimal range of 8–32 kPa. This not only enables stable dressing fixation but also safeguards wound integrity during replacement, laying a crucial performance foundation for its practical application as an integrated diagnosis and treatment dressing for acute wounds.

2.5. *In vitro* antibacterial activity and biocompatibility

Surface contaminants are prone to compromising the performance of wound dressings and wound management strategies; thus, antibacterial activity is regarded as an indispensable property for wound dressings.[47–49] The antibacterial efficacy of the KA-Ca^{2+}/Cu_2O@CuS composite hydrogel was assessed using the viable colony counting method based on the standard plate counting technique. Test bacterial strains encompassed Gram-positive *Staphylococcus aureus* (Fig. 4A and B) and Gram-negative *Escherichia coli* (Fig. 4C and D). Notably, the antibacterial activity of the composite hydrogel is primarily derived from the synergistic antibacterial mechanism of Cu_2O and CuS. All experiments were performed in quintuplicate, and the results were presented as mean values. As illustrated in Fig. 4E, in comparison with the control group (the untreated bacterial group), the KA-Ca^{2+}/Cu_2O@CuS composite hydrogel (gels-the hydrogel-treated experimental group), significantly inhibited bacterial growth, with inhibition rates of 93.8% against *Escherichia coli* and 91.6% against *Staphylococcus aureus*, respectively.

The synergistic antibacterial mechanism of the composite hydrogel is mainly achieved through the sustained release of Cu^{2+} from Cu_2O@CuS nanoparticles, which serves as the core antibacterial pathway. The sustained and controlled release of Cu^{2+} effectively addresses the inherent bactericidal limitations of single-component nanoparticles, such as excessive burst release of Cu^{2+} that triggers biotoxicity and insufficient long-term bactericidal efficiency. Consequently, the sustained Cu^{2+} release achieves a "1 + 1 > 2" enhancement in bactericidal efficiency by maintaining an effective antibacterial concentration for a long time while avoiding adverse effects on normal cells. Moreover, the combination of Cu_2O and CuS regulates the release rate of Cu^{2+}, enabling a reduced dosage of each nanoparticle and further minimizing cytotoxicity toward normal tissue cells. This favorable feature renders the composite hydrogel particularly suitable for the management of skin wound infections.

Biocompatibility is of paramount importance for hydrogel dressings that adhere closely to wound surfaces and are employed for integrated wound diagnosis and therapy.[50,51] Initially, the biocompatibility of the KA-Ca^{2+}/Cu_2O@CuS composite hydrogel was evaluated using a live/dead staining assay. As depicted in Fig. 4F, konjac glucomannan (KGM), a natural polysaccharide, inherently exhibits excellent biocompatibility and hydrophilicity. Following 24 h and 72 h of co-culture with the KA-Ca^{2+}/Cu_2O@CuS composite hydrogel, immunofluorescence observations revealed that all cells in the samples maintained a healthy growth status, confirming the composite hydrogel's superior cytocompatibility for application as a wound healing dressing. To verify the biosafety of the KA-Ca^{2+}/Cu_2O@CuS composite hydrogel at varying concentrations, a cytocompatibility assay was conducted: NIH_3T_3 cells were cultured in extracts of the KA-Ca^{2+}/Cu_2O@CuS composite hydrogel with different concentrations for 24 h to 72 h, and cell viability was assessed *via* the CCK-8 assay.[49] The results demonstrated that cell viability remained stably above 96% (Fig. 4G), further validating the excellent biocompatibility of the KA-Ca^{2+}/Cu_2O@CuS composite hydrogel. However, this study still has certain limitations, as a comprehensive and systematic evaluation of *in vivo* biosafety has not yet been performed. The excellent biocompatibility of the material is attributed to the sustained and controlled release of copper ions from Cu_2O@CuS for antibacterial activity, as well as the low and safe copper content in the system.

2.6. Hemostatic performance of the KA-Ca^{2+}/Cu_2O@CuS composite hydrogel

To evaluate the hemostatic efficacy of the KA-Ca^{2+}/Cu_2O@CuS composite hydrogel, a rat tail amputation model was established in this study (Fig. 5A). Four treatment groups were set up for comparative hemostatic testing on amputated rat tails, namely the untreated control group, gauze group, cotton group, and composite hydrogel dressing group. Concurrently, the intrinsic hemostatic mechanism of the hydrogel was

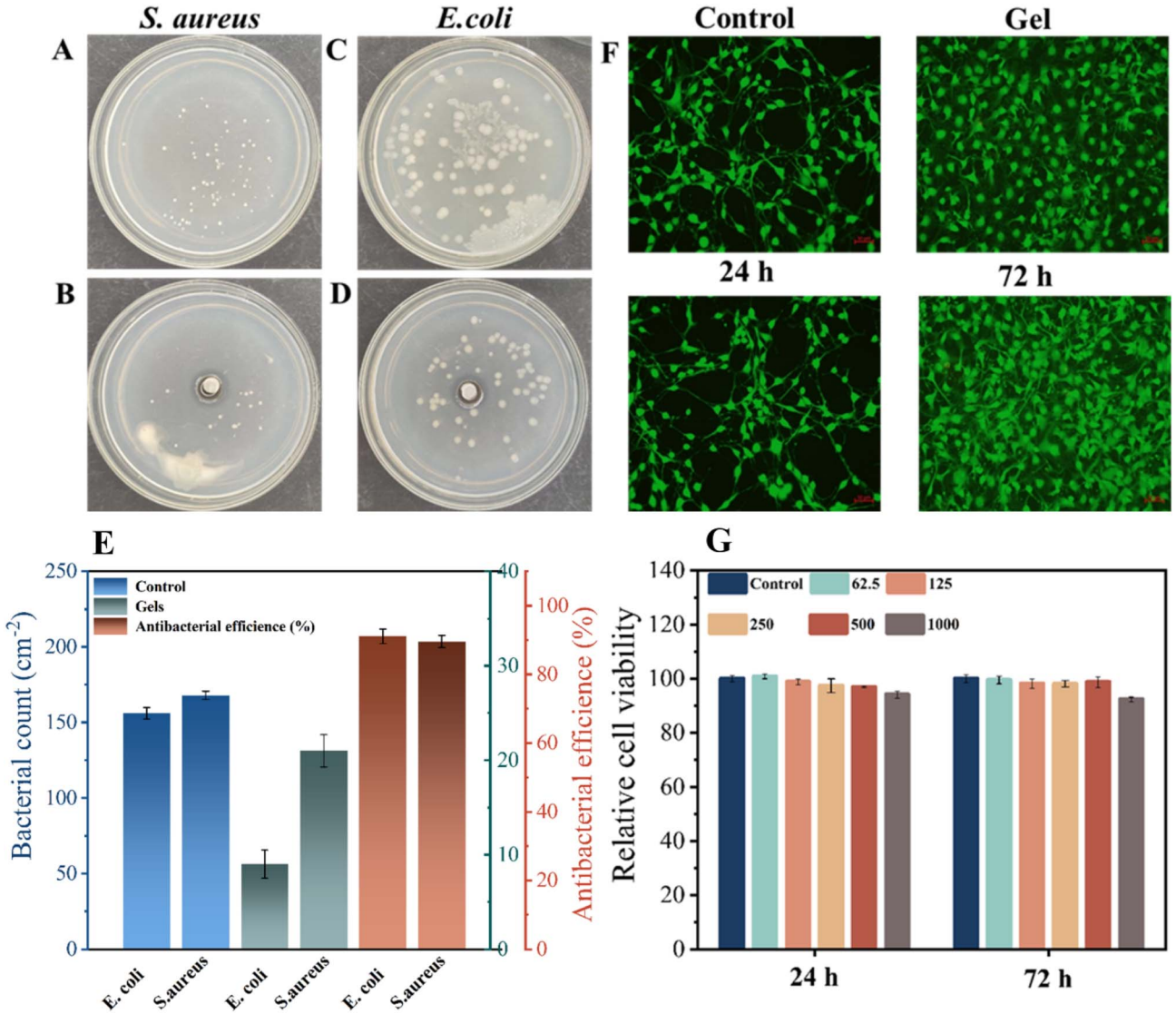

Fig. 4 Antibacterial properties and biocompatibility of hydrogels. (A and C) The antibacterial activities of the KA-Ca^{2+}/Cu_2O@CuS composite hydrogel against *Staphylococcus aureus* and *Escherichia coli* were evaluated separately using the spread plate method. (B and D) *Staphylococcus aureus* and *Escherichia coli* treated with the KA-Ca^{2+}/Cu_2O@CuS composite hydrogel. (E) Bacterial inhibition rates of the composite hydrogel against *Escherichia coli* and *Staphylococcus aureus*. (F) Live/dead cell imaging under a fluorescence microscope at 100× and 200× magnifications (green: live cells; red: dead cells), scale bar: 50 μm. (G) Cell viability of NIH3T3 cells co-cultured with KA-Ca^{2+}/Cu_2O@CuS hydrogel extracts at different concentrations for 24 h and 72 h.

comprehensively explored. The core hemostatic mechanism of the composite hydrogel is characterized as "blood-triggered swelling – firm adhesion – physical occlusion – synergistic coagulation promotion": upon contact with wound blood, the hydrogel promptly initiates a swelling response and firmly adheres to the bleeding site *via* intermolecular interactions. It achieves direct occlusion of blood flow through physical barrier formation, thereby facilitating the coagulation process (Fig. 5B).

This proposed mechanism was first corroborated by swelling experiments (Fig. 5D). Tests simulating various *in vivo* microenvironments (deionized water, normal saline, and tissue fluid) revealed that the maximum swelling ratios of the composite hydrogel were 549%, 443%, and 298%, respectively. These findings confirm that the composite hydrogel exhibits rapid swelling capacity for physical occlusion in the vascular injury microenvironment containing blood, which lays a robust foundation for its subsequent hemostatic performance.

With respect to the *in vitro* hemostatic outcomes (Fig. 5C, E and F), the amputated rat tails in the untreated control group displayed extensive bleeding on filter paper, with a blood loss of 0.18 ± 0.002 mg within 2 minutes and a prolonged hemostatic time of 570 ± 4 seconds. Although the gauze group showed a modest reduction in blood loss, the enhancement in hemostatic efficiency was marginal. The cotton group achieved partial bleeding control (blood loss: 0.06 ± 0.001 mg; hemostatic time: 162 ± 3 seconds), yet slight exudation persisted. In striking contrast, immediate application of the KA-Ca^{2+}/Cu_2O@CuS composite hydrogel to the wound post tail amputation resulted

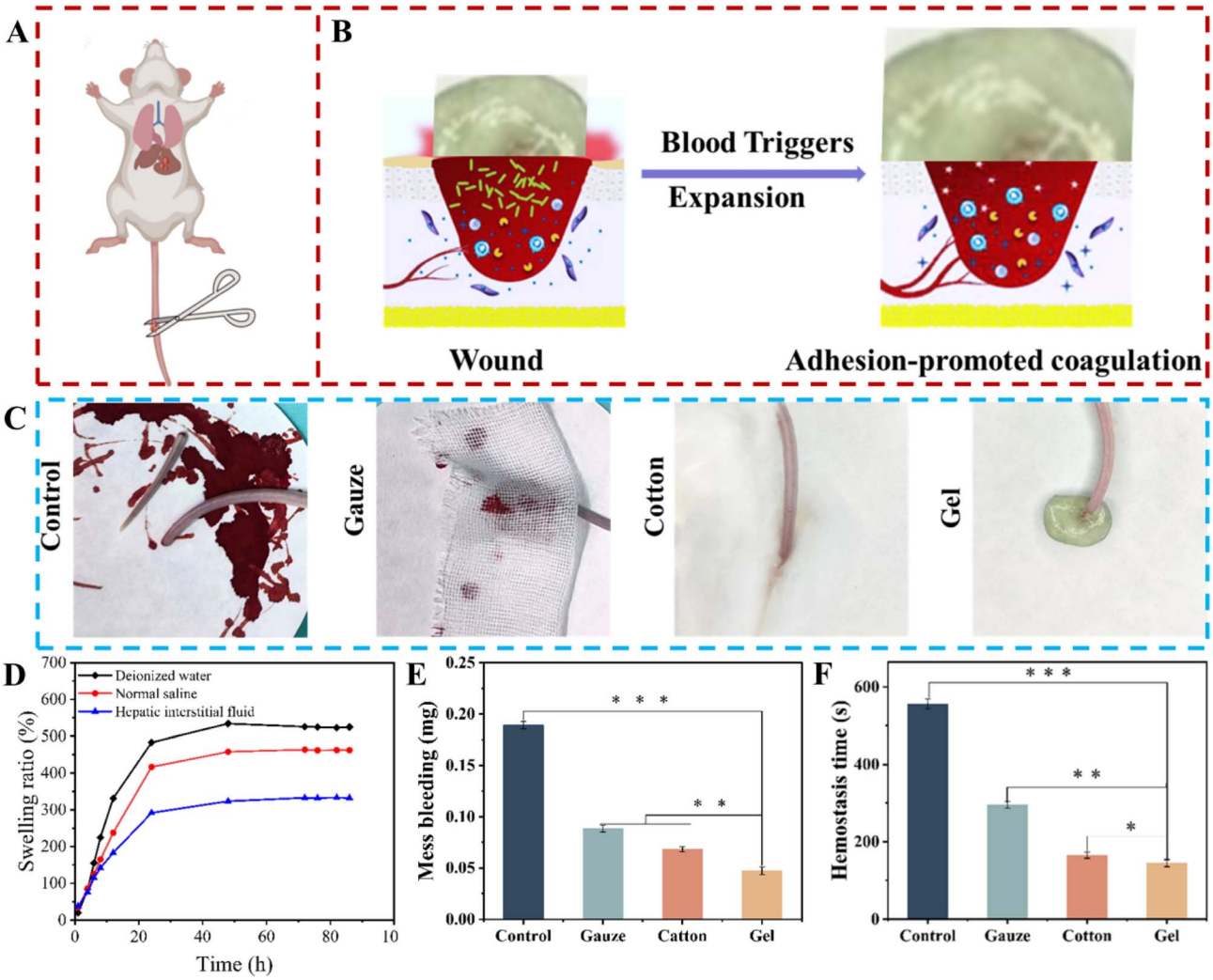

Fig. 5 Hemostatic performance of the hydrogel in a rat tail amputation model. (A) Schematic diagram of the bleeding and hemostasis model for rat tail amputation. (B) Schematic diagram of the hydrogel hemostatic mechanism. (C) Representative photographic records of hemostasis with different treatments on the amputated mouse tail. (D) Swelling performance of the composite hydrogel on different substrates. (E) Comparison of blood loss volume among different groups. (F) Comparison of hemostasis time among different groups. ($n = 3$, *$p < 0.05$, **$p < 0.01$, ***$p < 0.001$).

in nearly complete bleeding control within several seconds. Ultimately, the composite hydrogel group exhibited a remarkably shortened hemostatic time of 115 ± 2 seconds and a minimal blood loss of 0.04 ± 0.0037 mg within 2 minutes.

Collectively, the experimental data unequivocally demonstrate that the KA-Ca^{2+}/Cu_2O@CuS composite hydrogel significantly shortens hemostatic time and reduces blood loss *via* its core mechanism of "blood-triggered swelling – physical occlusion". Its hemostatic efficacy outperforms that of traditional hemostatic materials (gauze and cotton) and the blank control, indicating its great potential in achieving rapid hemostasis for acute wounds.

2.7. Wound healing evaluation of the KA-Ca^{2+}/Cu_2O@CuS composite hydrogel

Given the excellent tissue adhesion and efficient hemostatic properties of the KA-Ca^{2+}/Cu_2O@CuS composite hydrogel, this study established a timeline for the composite hydrogel-mediated wound treatment (Fig. 6A) and further investigated its promotional effect on skin wound healing using a 2 cm rat skin incision model (Fig. 6B). At the initial stage of the study, the adhesive performance of the hydrogel was verified experimentally: it could not only stably adhere to rigid substrates such as wood and glass but also tightly conform to the serosal layer, muscle layer, epidermal layer, and fat layer of porcine liver, porcine heart, and porcine skin under moist conditions (Fig. 3E). Notably, the hydrogel was capable of re-adhering two completely transected porcine skin segments. As illustrated in Fig. 6B, upon application to the wound, the KA-Ca^{2+}/Cu_2O@CuS composite hydrogel achieved complete wound coverage and occlusion through water absorption and swelling, thereby facilitating the reconnection of wound tissues. Observations on day 10 post-surgery revealed obvious and uneven scar hyperplasia in the untreated control group, whereas almost no scar

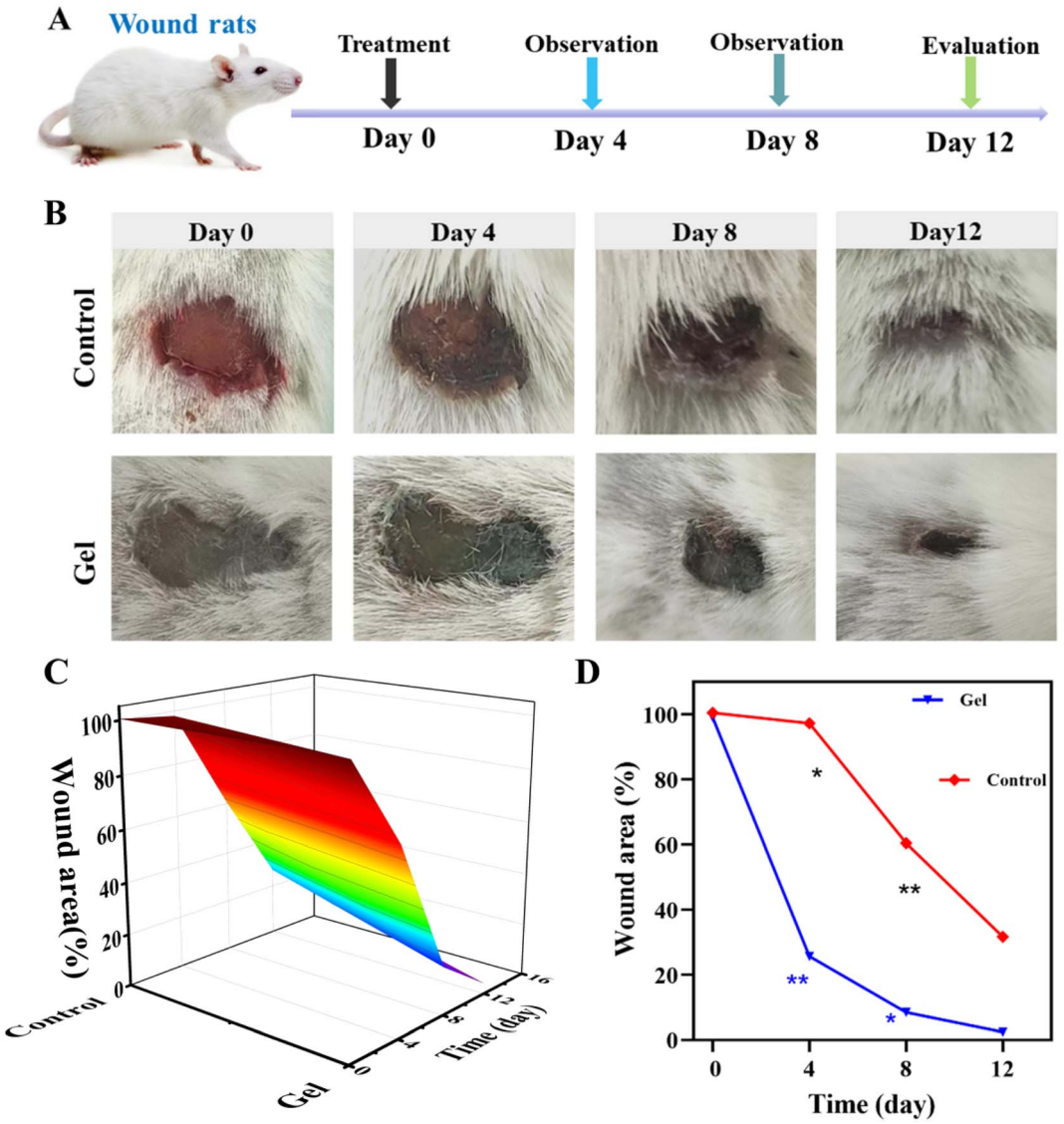

Fig. 6 To evaluate the wound healing-promoting performance of the KA-Ca^{2+}/Cu_2O@CuS composite hydrogel. (A) Timeline for composite hydrogel-treated wounds. (B) Wound images at different time points. (C) Simulated wound healing trajectory. (D) Quantitative analysis of wound area. Data are presented as mean ± standard deviation ($n = 3$). *$p < 0.05$, **$p < 0.01$, ***$p < 0.001$.

formation was observed in the KA-Ca^{2+}/Cu_2O@CuS composite hydrogel-treated group. Meanwhile, the regeneration of new epidermis and hair in the hydrogel-treated group was significantly improved compared with the control group. These experimental results fully demonstrate that the KA-Ca^{2+}/Cu_2O@CuS composite hydrogel can significantly enhance the quality of wound healing.

To further confirm the promotional efficacy of the KA-Ca^{2+}/Cu_2O@CuS composite hydrogel in tissue regeneration, a continuous observation period of 12 days was conducted in this study. The results showed that the wound closure rate in the KA-Ca^{2+}/Cu_2O@CuS composite hydrogel-treated group was consistently higher than that in the control group throughout the entire observation period (Fig. 6C). After 12 days of treatment, the wounds in the KA-Ca^{2+}/Cu_2O@CuS composite hydrogel-treated group had achieved almost complete healing, with a healing area of 98.3% ± 3.5%. In contrast, the wound closure rate in the control group was only 76.5% ± 4.8% (Fig. 6D).

It is well recognized that natural polysaccharide-based materials possess favorable biocompatibility. The present study further confirmed that the KA-Ca^{2+}/Cu_2O@CuS composite hydrogel not only exhibits robust wet tissue adhesion and adequate structural stability but also has inherent cell and tissue affinity. Specifically, the abundant hydroxyl and amino groups in the molecular structure of the composite hydrogel endow it with strong binding affinity to various nucleophilic groups on the tissue surface (including hydrogen bonding and ionic bonding interactions), thereby enhancing its tissue adhesion efficacy. In addition, benefiting from its porous structural characteristics, the KA-Ca^{2+}/Cu_2O@CuS composite hydrogel can rapidly absorb exudates from the injured site upon

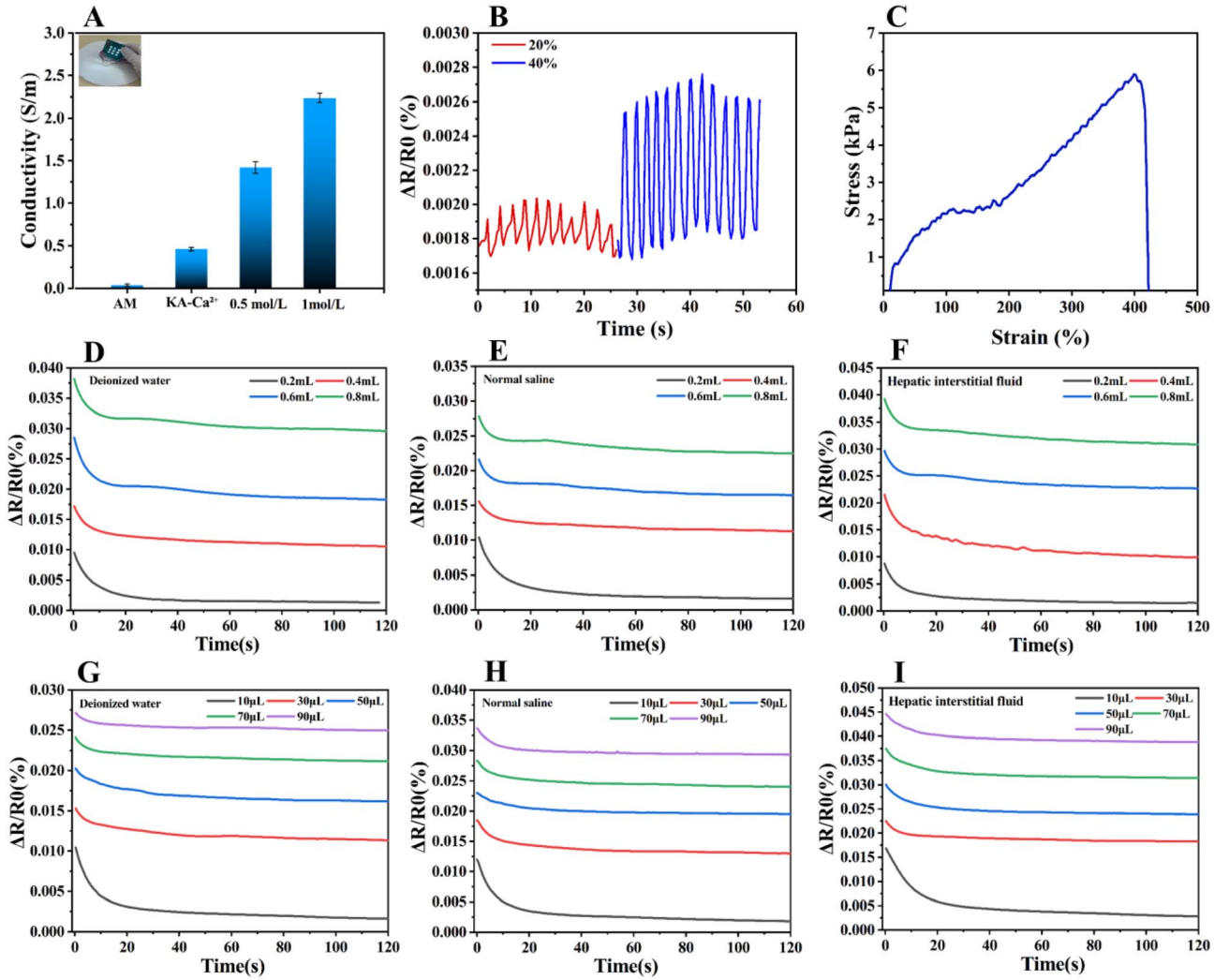

Fig. 7 Sensing performance of the KA-Ca^{2+}/Cu_2O@CuS composite hydrogel (including tearing, different types and concentrations of exudates): (A) electrical conductivity. (B) Response of the hydrogel to tearing strain. (C) Tensile strength. Responses of the hydrogel to 0.2–0.8 mL and 10–90 μL exudates: (D and G) deionized water; (E and H) normal saline; (F and I) tissue fluid.

application to the wound, and then form a protective layer with procoagulant function through the synergistic effect of "swelling–adhesion–occlusion". The synergistic effect of these multiple properties collectively enhances the wound healing-promoting capacity of the KA-Ca^{2+}/Cu_2O@CuS composite hydrogel.

2.8. Sensing performance of the composite hydrogel

The electrical conductivity of the KA-Ca^{2+}/Cu_2O@CuS composite hydrogel was evaluated *via* an electrochemical workstation, with the corresponding results presented in Fig. 7A. The hydrogel without Cu_2O@CuS nanoparticles exhibited relatively low electrical conductivity; specifically, the pristine AM hydrogel showed a conductivity value of merely 0.04 S m^{-1}. Benefiting from the cross-linking effect of Ca^{2+} ions, the conductivity of the KA-Ca^{2+} hydrogel increased to 0.46 S m^{-1}. Nevertheless, the incorporation of Cu_2O@CuS nanoparticles significantly enhanced the electrical conductivity of the hydrogel. With the increase in Cu_2O@CuS nanoparticle content, the conductivity of the hydrogel increased steadily, and the KA-Ca^{2+}/Cu_2O@CuS hydrogel with a nanoparticle concentration of 1 mol L^{-1} achieved a maximum conductivity of 2.24 S m^{-1}. These findings highlight the effectiveness of Cu_2O@CuS nanoparticles in boosting the electrical conductivity of the hydrogel. The superior electrical conductivity of the KA-Ca^{2+}/Cu_2O@CuS composite hydrogel indicates its great potential for wound status monitoring, rendering it a promising candidate material for flexible skin sensors.

Accumulating evidence has confirmed that the occurrence of skin infections is likely to induce alterations in temperature or humidity. Additionally, external tearing forces can, to a certain extent, reflect the surface status of wounds. As documented in the literature, mechanical trauma induced by external tearing can exacerbate tissue damage and lead to scar hyperplasia or impaired healing by triggering excessive inflammatory responses, compromising the functions of fibroblasts and

vascular endothelial cells, and disrupting the alignment of collagen fibers as well as the homeostasis of collagen metabolism. Consequently, effective management of external tearing forces is crucial for mitigating wound inflammation and oxidative stress. Given the remarkable electrical conductivity and biocompatibility of the KA-Ca^{2+}/Cu_2O@CuS composite hydrogel, this sensor is expected to monitor changes in external tearing forces and exudates (wound humidity) for the prevention of skin damage and infections.

Herein, a skin sensor based on the KA-Ca^{2+}/Cu_2O@CuS composite hydrogel was fabricated to monitor two critical indicators of acute wound healing: exudates with varying types and concentrations, and external tearing forces. As illustrated in Fig. 7B, the $\Delta R/R_0$ value of the KA-Ca^{2+}/Cu_2O@CuS composite hydrogel increased progressively with the applied strain in the 20–40% tensile-release range. The variation in $\Delta R/R_0$ value was well-correlated with the applied strain, exhibiting a consistent dose–response relationship. The skin sensor stably yielded $\Delta R/R_0$ values of 0.0019% and 0.0027%, respectively, demonstrating prominent repeatability and sensitivity toward changes in external tearing forces. Fig. 7C verifies the excellent tensile properties of the hydrogel; such features not only guarantee monitoring accuracy but also prolong the service life of the flexible skin sensor.

Deionized water, normal saline, and tissue fluids with varying concentrations were extruded *via* a syringe to simulate acute wound exudates, as illustrated in Fig. 7D–I. Fig. 7D–F depict the relative resistance changes of the flexible sensor in response to different types of exudates (deionized water, normal saline, and tissue fluid) within the volume range of 0.2–0.8 mL. Notably, Fig. 7G–I demonstrate the rapid response of the sensor to trace volumes (10–90 μL) of different exudate types. Collectively, these findings confirm the potential of the composite hydrogel for monitoring multiple parameters, including external tearing forces and exudates with varying types and concentrations, thereby providing critical performance support for the practical implementation of integrated diagnosis and treatment dressings for acute wounds.

3 Conclusions

In summary, addressing critical clinical bottlenecks of delayed hemostasis and high infection risk in wounds, this study developed a KA-Ca^{2+}/Cu_2O@CuS composite hydrogel based on the demand for integrated diagnosis-treatment of acute wounds. Fabricated *via* Ca^{2+}–mediated crosslinking of KGM/AM matrix with Cu_2O@CuS loading, the hydrogel integrates swelling–adhesion, antibacterial, conductive, and procoagulant properties. Endowed with the "blood-triggered swelling–occlusion–adhesion–sealing–procoagulation" mechanism, it exhibits excellent hemostatic efficacy (115 s in rat tail amputation), broad-spectrum antibacterial activity (>96% inhibition against *S. aureus* and *E. coli*), and wound monitoring potential. With a tissue fluid swelling ratio of 287%, porcine skin adhesion strength of 26.3 kPa, and good biocompatibility (max NIH3T3 survival rate 98%), it significantly promotes wound healing (98.3% healing area on day 12 in rat model). Compared with traditional materials, its integrated "hemostasis-antibacterial-healing promotion-monitoring" advantages enhance diagnosis-treatment efficacy remarkably, showing great prospects in complex clinical wounds. Its conductivity also lays a foundation for intelligent devices, making it a promising candidate for acute wound management.

4 Experimental section

4.1. Materials (experimental materials in SI)

4.1.1 Preparation of KA-Ca^{2+}/Cu_2O@CuS hydrogel

4.1.1.1 Synthesis of Cu_2O@CuS. The synthesis of Cu_2O@CuS nanocubes was performed as follows: polyethylene glycol (PEG) served as the capping agent, sodium borohydride ($NaBH_4$) as the primary reducing agent, and ascorbic acid as the antioxidant, with sodium hydroxide (NaOH) used to adjust the pH of the reaction system. At the initial synthesis stage, 1.25 g of $CuSO_4 \cdot 5H_2O$ was dissolved in 50 mL of deionized water to form a blue solution. A 50 mL deionized water solution containing 6 g of PEG was then added to this blue solution under vigorous stirring, resulting in a white solution. Subsequently, a 100 mL deionized water solution containing 0.9 g of ascorbic acid and 0.4 g of NaOH was introduced into the aforementioned mixture, followed by the dropwise addition of a 50 mL aqueous solution of 0.4 g $NaBH_4$. Continuous stirring produced a dark red solution, which was allowed to stand and cool overnight, leading to a color change to yellow. Copper(I) oxide (Cu_2O) nanocubes were harvested *via* centrifugation, washing, and drying processes. The as-prepared Cu_2O nanocubes were dispersed in 150 mL of deionized water, and 0.065 g of Na_2S was added under constant stirring. After a 1 hour reaction, the dark red product was collected by centrifugation and dried in a vacuum oven at 60 °C to obtain Cu_2O@CuS nanocubes, which were reserved for subsequent experiments.

4.1.1.2 Fabrication of the KA-Ca^{2+}/Cu_2O@CuS hydrogel. The preparation procedure for the KA-Ca^{2+}/Cu_2O@CuS nanohydrogel matrix was conducted as follows: initially, 3.5 g of acrylamide (AM) and 0.02 g of home-synthesized copper(I) oxide@copper sulfide (Cu_2O@CuS) were co-dissolved in 10 mL of deionized water. Subsequently, 0.35 g of konjac glucomannan (KGM) was added to the mixture, which was then stirred until homogeneous. Thereafter, a cross-linker solution, prepared by dissolving 0.5 g of calcium chloride ($CaCl_2$) in 2 mL of deionized water, was introduced, followed by the addition of 1 mL of an aqueous solution containing 0.1 g of ammonium persulfate (APS) to initiate polymerization. Finally, the resulting mixture was poured into a Petri dish and incubated in an oven at 60 °C. After a 20 minute reaction, the target hydrogel was successfully fabricated.

Other specific methods are in the SI (4.1–4.9)

Author contributions

Qin Wang: first writing and data analysis. Linfeng Shi: data analysis. Yuqin Li: data curation. Xiuyu Liang: visualization. Zhongnan Wang: visualization. Gui Ma: supervision. Enke

Feng: conceptualization. Zhiming Yang: investigation, methodology. Lili Tian: software, writing-original draft preparation.

Conflicts of interest

The authors declare that they have no known competing financial interests or personal relationships that could have appeared to influence the work reported in this paper.

Data availability

All data underpinning the study conclusions are presented in the main text. Comprehensive details, including experimental protocols, characterization techniques and self-healing mechanism, are provided in the supplementary information (SI). Supplementary information is available. See DOI: https://doi.org/10.1039/d6ra01581f.

Acknowledgements

This work was financially funded by Guyuan Municipal Research and Development Science and Technology Program Project (2024BGTYF01-50, 2025GKJYF0018), Ningxia Natural Science Foundation (2026A0681)and Research Program of Ningxia Key Laboratory of Green Catalytic Materials and Technology (2025SYSYB-22).

References

1 Y. Wang, K. Nuutila, A. H. Carlsson, S. Christy, D. Larson, X. Li, Y. Chen, O. Hasturk, C. Li, R. Chan and D. Kaplan, *Adv. Funct. Mater.*, 2025, **35**(25), 2422888.
2 J. Yang, C. Long, K. Liu, X. Lu, J. Zhao, J. Hong, R. Zhang, S. Xia, Y. Qing, M. Yu and Y. Zhao, *Int. J. Biol. Macromol.*, 2024, **273**, 133075.
3 C. Wang, C. Shi, J. Huang, X. Wei, Y. Shi, L. Xiao and J. Fan, *ACS Appl. Mater. Interfaces*, 2024, **16**, 49186–49196.
4 F. Graham, *Nature*, 2024, **10**, 14.
5 P. Wang, Y. Pu, Y. Ren, W. Kong, L. Xu, W. Zhang, T. Shi, J. Ma, S. Li, X. Tan and B. Chi, *Int. J. Biol. Macromol.*, 2023, **226**, 813–822.
6 M. A. Mofazzal Jahromi, P. Sahandi Zangabad, S. M. Moosavi Basri, K. Sahandi Zangabad, A. Ghamarypour, A. R. Aref, M. Karimi and M. R. Hamblin, *Adv. Drug Delivery Rev.*, 2018, **123**, 33–64.
7 J. Zhu, K. Zhang, Y. Zhang, C. Zhou, Z. Cui, W. Li, Y. Wang and J. Qin, *Int. J. Biol. Macromol.*, 2024, **282**, 137323.
8 Y. Huang, L. Bai, Y. Yang, Z. Yin and B. Guo, *J. Colloid Interface Sci.*, 2022, **608**, 2278–2289.
9 K. L. J. S. Christman, *SCIENCE*, 2019, **363**, 340–341.
10 L. A. Dempsey, *Nat. Immunol.*, 2023, **24**, 1051.
11 S. Bi, C. He, Y. Zhou, R. Liu, C. Chen, X. Zhao, L. Zhang, Y. Cen, J. Gu and B. Yan, *Biomaterials*, 2025, 314.
12 L. Deng, Y. Cheng, J. Liu, Y. Yuan, C. Zhou, C. Yao, J. Sun, Z. Zhou, Z. Chen, Z. Wang and L. Wang, *J. Nanobiotechnol.*, 2025, **23**(1), 456.
13 T. Aihara, I. Hayakawa, K. Ide and Y. Abe, *J. Neurol. Sci.*, 2024, **465**, 6.
14 W. You, Z. Cai, F. Xiao, J. Zhao, X. Yu, W. Wang, Z. Chen, W. Hu, G. Sun and Z. Wang, *Chem. Eng. J.*, 2024, **498**, 155722.
15 G. Zheng, J. Xie, Y. Yao, S. Shen, J. Weng, Q. Yang and Q. Yan, *ACS Appl. Mater. Interfaces*, 2024, **16**(10), 12202–12216.
16 Y. Kang, K. Liu, Z. Chen, J. Guo, K. Xiang, X. Wu, T. Jiang, J. Chen, C. Yan, G. Jiang, Y. Wang, M. Zhang, X. Xiang, H. Dai and X. Yang, *J. Controlled Release*, 2024, **370**, 210–229.
17 A. Osmokrovic, J. Stojkovska, T. Krunic, P. Petrovic, V. Lazic and J. Zvicer, *Int. J. Mol. Sci.*, 2025, **26**, 4381.
18 T. Zhao, R. Ren, S. Qiao, X. Tang, Z. Chi, F. Jiang and C. Liu, *J. Colloid Interface Sci.*, 2025, **683**, 828–844.
19 H. He, C. Sun, Y. Weng, H. Huang, P. Ni, Y. Fang, R. Xu, Z. Wang and H. Liu, *Carbohydr. Polym.*, 2022, **286**, 119319.
20 X. Wu, C. Wang, J. Wang, Y. Feng, Y. Zhu, Y. Pan, Y. Yuan, C. Chen, J. Cao, J. Lin, X. Tong, Y. Li, C. Wen, X. Shen and J. Ma, *Chem. Eng. J.*, 2024, **491**, 152060.
21 J. Liu, H. Cheng, X. Yuan, L. Wang and J. J. C. Gao, *Cellulose*, 2024, **31**, 7613–7627.
22 Y. Sun, H. Fu, Y. Xu, T. Chen, Z. Liu, X. Liu and W. Bing, *React. Funct. Polym.*, 2024, **203**, 106020.
23 P. Liu, J. Wang, Y. Wang, Y. Bai, H. Zhou and L. Yang, *Biomater. Sci.*, 2024, **12**, 3193–3201.
24 L. Tian, T. Liu, Y. Jiang, B. He and H. Hao, *Chem. Eng. J.*, 2024, **497**, 154890.
25 R. Ding, X. Xu, H. Ding, Z. Chen, H. Xia, S. Cao, Z. Gu and H. Mao, *ACS Appl. Mater. Interfaces*, 2025, **17**, 60255–60268.
26 L. L. Dai, Y. Geng, X. F. Ding, Z. K. Zhang, C. H. Lai, D. H. Zhang, C. L. Xia and Y. X. Lai, *Carbohydr. Polym.*, 2025, **366**, 10.
27 Y. X. Huang, J. Hu, Y. H. Zhang, Y. L. Yu, D. H. Zhang, Q. M. Jing, M. W. Shahzad, S. Donkor, C. Chen, C. W. Zhang, X. M. He, B. B. Xu, S. B. Ge and W. J. Yu, *Adv. Mater.*, 2026, **38**, 31.
28 C.-Y. Zou, C. Han, F. Xing, Y.-L. Jiang, M. Xiong, J. Li-Ling and H.-Q. Xie, *Bioact. Mater.*, 2025, **45**, 459–478.
29 Y. Zhang, M. Li, J. Chang, C. Li, Y. Hui, Y. Wang, W. J. B. Xu and Trauma, *Burns & Trauma*, 2024, p. 12.
30 Y. Jiang, C. Zhu, X. Ma and D. Fan, *Chem. Eng. J.*, 2024, **500**, 157139.
31 T. Liu, H. Lei, L. Qu, C. Zhu, X. Ma and D. J. C. P. Fan, *Carbohydr. Polym.*, 2025, **347**, 122751.
32 L. Tian, B. He, Y. Liu, Q. Zhang, S. Liang, Y. Yuan, Q. Han, S. Ju, L. Cong and C. Cai, *ACS Appl. Polym. Mater.*, 2024, **6**, 9099–9109.
33 S. Wei, X. Liu, J. Zhou, J. Zhang, A. Dong, P. Huang, W. Wang and L. Deng, *Int. J. Biol. Macromol.*, 2020, **155**, 153–162.
34 P. Choudhary, B. Ramalingam, S. Bose and S. K. Das, *Biomater. Sci.*, 2025, **13**, 639–658.
35 P.-F. Cai, B.-D. Zheng, Y.-L. Xu, B.-X. Li, Z.-Y. Liu, Y.-Y. Huang, J. Ye and M.-T. Xiao, *Int. J. Biol. Macromol.*, 2024, **266**, 131179.
36 A. Wang, G. Fan, H. Qi, H. Li, C. Pang, Z. Zhu, S. Ji, H. Liang, B.-P. Jiang and X.-C. Shen, *Biomaterials*, 2022, **289**, 121798.
37 D. Li, X. Fei, L. Xu, Y. Wang, J. Tian and Y. Li, *J. Colloid Interface Sci.*, 2022, **627**, 942–955.

38 Z. Wang, B. Qi, R. Wang, Z. Chen, J. Zhong, Z. Wang, Q. Sun, A. Yu, X. Shen and H. Xie, *Chem. Eng. J.*, 2025, **520**, 166108.
39 J. Wang, C. Zhao, P. Yang, H. He, Y. Yang, Z. Lan, W. Guo, Y. Qin, Q. Zhang and S. Li, *J. Colloid Interface Sci.*, 2025, **679**, 737–747.
40 D. Yang, Y. Yuan, L. Wang, X. Wang, R. Mu, J. Pang, J. Xiao and Y. Zheng, *Int. J. Mol. Sci.*, 2017, **18**, 2250.
41 A. Zhang, Y. Liu, D. Qin, M. Sun, T. Wang and X. Chen, *Int. J. Biol. Macromol.*, 2020, **164**, 2108–2123.
42 P. Nezhad-Mokhtari, M. Hasany, M. Kohestanian, A. Dolatshahi-Pirouz, M. Milani and M. Mehrali, *Adv. Colloid Interface Sci.*, 2024, **334**, 103306.
43 X. Chai, R. Ge, Y. Lou, F. M. U. Turaqulov, K. E. Yunusov, L. Nie, M. R. Khan and G. Jiang, *Chem. Eng. J.*, 2025, **525**, 169775.
44 J. Tian, Y. Zhang, L. Yang, L. Wang, G. Ling and P. Zhang, *ACS Appl. Polym. Mater.*, 2025, **7**(17), 11091–11104.
45 M. John, J. Park and K. Kirane, *Compos. Appl. Sci. Manuf.*, 2024, **185**, 108368.
46 Z. Zhang, Y. Zhang, Y. Liu, P. Zheng, T. Gao, B. Luo, X. Liu, F. Ma, J. Wang and R. J. S. C. Pei, *Sci. China Mater.*, 2023, **66**, 3337–3346.
47 S. Tan, X. Yuan, Z. Song, Z. Lin, F. Zhao, L. Wang and J. Gao, *Chem. Eng. J.*, 2024, **500**, 500.
48 X. Liu, Y. Sun, J. Wang, Y. Kang, Z. Wang, W. Cao, J. Ye and C. J. B. M. Gao, *Bioact. Mater.*, 2024, **34**, 269–281.
49 Y. Wang, Q. Ma, B. Zheng, W. Xiong, D. Miao, Y. Li, R. Huang, H. Wang and D. Wu, *Adv. Mater.*, 2025, **37**(10), 2413320.
50 Z. Miao, Y. Sun, Z. Tao, Y. Chen, Y. Ma, D. Zhu, X. Huang and Z. Zha, *Adv. Healthcare Mater.*, 2021, **10**(18), 2170081.
51 Y. Liu, X. Ren, Y. Zheng, M. Yin and M. Zuo, *Mater. Des.*, 2025, **257**, 114503.